Cold-start emissions control in hybrid vehicles equipped with a passive adsorber for hydrocarbons and nitrogen oxides

Article *in* Proceedings of the Institution of Mechanical Engineers Part D Journal of Automobile Engineering · October 2012

DOI: 10.1177/0954407012443764

CITATIONS
24

READS
629

6 authors, including:

Zhiming Gao
Battelle Memorial Institute
71 PUBLICATIONS **1,356** CITATIONS
SEE PROFILE

Jae-Soon Choi
Oak Ridge National Laboratory
63 PUBLICATIONS **1,496** CITATIONS
SEE PROFILE

Stuart Daw
Oak Ridge National Laboratory
232 PUBLICATIONS **4,774** CITATIONS
SEE PROFILE

James E. Parks II
Oak Ridge National Laboratory
72 PUBLICATIONS **2,047** CITATIONS
SEE PROFILE

Original Article

Institution of MECHANICAL ENGINEERS
Journal of AUTOMOBILE ENGINEERING

Proc IMechE Part D:
J Automobile Engineering
226(10) 1396–1407

DOI: 10.1177/0954407012443764
pid.sagepub.com
SAGE

Cold-start emissions control in hybrid vehicles equipped with a passive adsorber for hydrocarbons and nitrogen oxides

Zhiming Gao, Mi-Young Kim, Jae-Soon Choi, C Stuart Daw, James E Parks II and David E Smith

Abstract

We present results from a computational study of the potential for using low-cost sorbent materials to trap the emissions of hydrocarbons and nitrogen oxides temporally during cold-start periods in hybrid electric vehicles and plug-in hybrid electric vehicles operating over transient driving cycles. The hydrocarbon adsorption behavior of a candidate sorbent composed of Ag-beta-zeolite was characterized in a laboratory flow reactor to estimate the kinetic parameters for a one-dimensional transient adsorber device model. This model was then implemented in the Powertrain Systems Analysis Toolkit to simulate a passive hydrocarbon adsorber device on a hybrid vehicle. The results indicate that such an adsorber can substantially reduce the hydrocarbon emissions by temporarily storing them until the three-way catalyst is sufficiently warm to remove them from the exhaust. A similar adsorber device model was simulated for nitrogen oxide control, using an initial set of conjectured kinetic parameters for transition metal oxides based on limited information in the literature. These latter simulations revealed the need to pursue additional experimental studies to characterize fully this class of sorbents. Such studies are especially relevant in the present context of rapidly evolving vehicle technology, because emission controls of this type do not involve any penalty in fuel consumption or require any change in engine operation.

Keywords

Cold start, emissions control, passive adsorber, hybrid electric vehicle

Date received: 1 October 2011; accepted: 2 March 2012

Introduction

Hybrid electric vehicles (HEVs) and plug-in hybrid electric vehicles (PHEVs) offer substantial benefits for improved fuel economy, carbon dioxide (CO_2) emission reduction, and petroleum displacement. However, intermittent utilization of the combustion engine in HEVs and PHEVs increases the impact of cold-start emissions. Three-way catalysts (TWCs) are widely used for controlling the emissions from conventional gasoline engines but are effective only when the catalyst temperature reaches a critical 'light-off' threshold. For current TWCs, this threshold is about 150–200 °C.[1,2] Recently, there has been considerable interest in developing catalysts that become active at lower temperatures.[3–5] Since a cold start always involves a delay in catalyst heat-up, there can be a significant release of carbon monoxide (CO), unburned hydrocarbons (HCs), and nitrogen oxides (NO_x) before the catalyst becomes functional. In conventional vehicles, a cold start can contribute up to 80–90% of the total drive cycle emissions during the 30–40 s required to heat up the catalyst.[2,6] Thus a cold start is a major concern for HEVs and PHEVs, where engine operation is typically much more intermittent. This provides a major motivation for developing innovative technologies for reducing cold-start emissions from hybrid vehicles.

Several approaches have been proposed to heat up the emission control systems rapidly in conventional vehicles, including direct catalyst heating[6,7] and rapid ramping of the engine fueling rate.[8–10] These methods

Oak Ridge National Laboratory, Oak Ridge, Tennessee, USA

Corresponding author:
Zhiming Gao, Oak Ridge National Laboratory, PO Box 2008 MS 6472, Oak Ridge, TN 37831-6472, USA.
Email: gaoz@ornl.gov

suffer from the disadvantage that they consume fuel or battery power to generate the added heat, thus negatively impacting the overall energy efficiency. Other studies have focused on developing catalysts that function more effectively at low temperatures, e.g. by exploiting the properties of gold nanoparticles.[11,12] Unfortunately, deactivation and poor long-term stability become issues for these catalysts under realistic exhaust conditions.

A third approach for controlling cold-start emissions utilizes low-temperature adsorption (we use this term to refer to both physical adsorption and chemical adsorption) to capture pollutants temporarily until the catalyst is sufficiently heated. Low-temperature adsorption has been considered for controlling a wide range of emissions in the chemical industry, including CO, HC, and NO_x.[13–16] Low-temperature adsorbers have also been investigated in automotive applications. For example, zeolites have been used to trap and then to release HCs once the after-treatment system is sufficiently heated.[13,14,17,18] Such adsorbers have the advantage that they do not consume additional fuel or battery energy, and they are relatively inexpensive compared with precious metal catalysts (e.g. less than US$1.0 per gram). The amount of sorbent material required to trap the emissions during the cold-start period is also typically much less than that required in catalytic devices, so that the added volume of adsorber devices is comparatively small.

Recent studies of passive adsorbers have focused mainly on HCs, with candidate sorbent materials such as Ag-beta-zeolite of high interest because of the capacity of its large pores to capture large molecules,[1] but there are also efforts under way to develop improved sorbent materials for other exhaust species such as NO_x. In particular, Fe–Mn–Zr transition metal oxides have been reported to have a high NO_x adsorption capacity at ambient temperature in the presence of oxygen.[1,15] In Fe-Mn-Zr oxides, it appears that ZrO_2 adsorbs NO_2, while FeO_x and MnO_x catalyze NO oxidation to NO_2. Both of these sorbents can be regenerated (releasing their adsorbates) when heated above 150 °C.[15] Although NO_x adsorption by transition metal oxides has been studied in the laboratory under the conditions relevant to the chemical industry, we have not been able to find reports concerning their utilization for vehicle cold-start emission controls.

In this paper we summarize results from a preliminary study of the potential for using chemisorbing materials to trap the HC emissions and the NO_x emissions respectively temporally during cold-start periods in HEVs and PHEVs over transient driving cycles. As far as we are aware, this is the first study in which a direct link between the adsorbent properties and the dynamic drive cycle tailpipe emissions from hybrid vehicles has been reported in the open literature. As a basis for our HC capture modeling, we made laboratory measurements with a model Ag-beta-zeolite sorbent to characterize its adsorption and desorption behavior. We then parameterized a simple sorbent model with kinetic rate constants derived from the experimental measurements, which were then utilized in a one-dimensional transient device model implemented in the Powertrain Systems Analysis Toolkit (PSAT)[19] to simulate the impact of a passive adsorber device on the HC emissions from a gasoline-powered passenger HEV and a gasoline-powered passenger PHEV. Preliminary kinetic parameters were also proposed for a transition metal NO sorbent based on limited information in the literature. These parameters were then used to simulate a passive NO adsorber on an HEV and a PHEV also. The impact of the large uncertainty in these latter parameters on the simulated performance reveals how important it is to carry out further detailed laboratory studies on such materials.

For conducting the PSAT simulations, we utilized a previously published methodology to account for the emissions and temperature transients in the engine exhaust.[20] We also utilized a previously published TWC model developed at Oak Ridge National Laboratory[21] to simulate the performance of a TWC.

Experimental methods

The experimental HC adsorber materials considered in the present study included Ag-ZSM-5 and Ag-beta-zeolites. These were prepared by ion exchange of ZSM-5 and beta-zeolites respectively from Zeolyst, with an aqueous solution of $AgNO_3$ (15 cm^3 $AgNO_3$/g zeolite) at 60 °C for 7 h. After the exchange, the solutions were filtered and washed with deionized water. The silver-exchanged solids were dried overnight at 100 °C and then calcined at 550 °C for 8 h. The Ag-ZSM-5 had a silicon-to-aluminum ratio of 15 and a surface area of 400 m^2/g, while the Ag-beta-zeolite had a silicon-to-aluminum ratio of 12.5 and a surface area of 680 m^2/g.

The adsorption and desorption behavior of the above sorbents exposed to propylene (C_3H_6) was characterized with a fixed-bed quartz reactor of 10 mm diameter (Figure 1). Samples of sorbent materials were placed in a U-shaped quartz reactor between two plugs of quartz wool, which was suspended in the heated

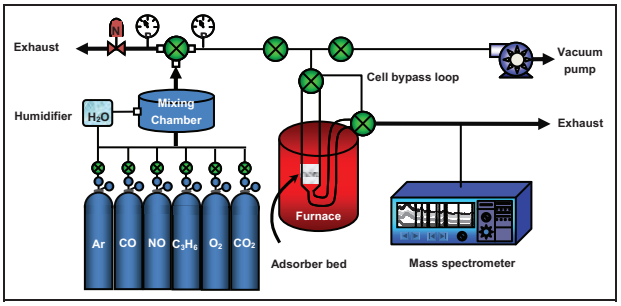

Figure 1. Schematic diagram of the experimental fixed-bed sorber used for characterizing C_3H_6 adsorption and desorption behavior.

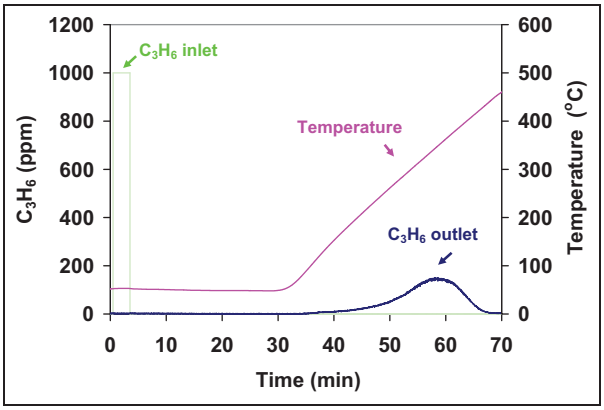

Figure 2. Experimental HC breakthrough curve for the fixed-bed sorber containing beta-zeolite. For adsorption, a 3 min concentration step of 1000 ppm C_3H_6 was injected into the 200 cm^3/min argon stream (52,000 h^{-1} space velocity). The desorption temperature ramp was initiated 30 min later.

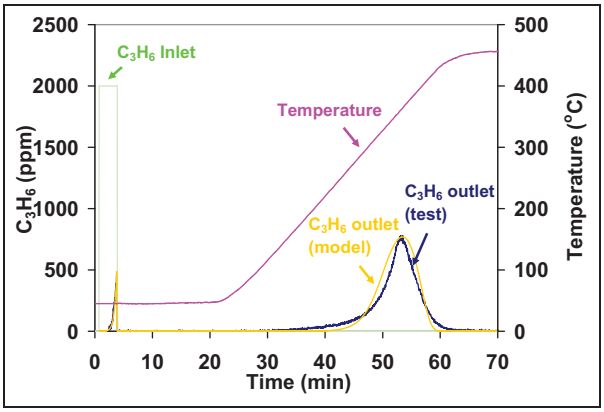

Figure 3. Measured and simulated HC breakthrough profiles for the fixed-bed sorber containing a mixed sorbent and fed with simulated exhaust. The adsorbing stage consisted of an inlet step in a C_3H_6 concentration of 2000 ppm, with 2000 ppm CO, 325 ppm NO, 2% H_2O, 2% O_2, 4% CO_2 in a balance of argon in the carrier gas for 3 min at 50 °C followed by argon only and a temperature ramp of 10 °C/min. The carrier gas flow was 200 cm^3/min, yielding a space velocity of 34,000 h^{-1}.

zone. The temperature was managed by a programmable temperature controller. Each powder sample was pre-treated at 450 °C under argon flow and then cooled to 45 °C. The samples were then exposed to a total flow of 200 ml/min argon or simulated exhaust gas mixtures with 3 min step inputs of 1000 ppm or 2000 ppm C_3H_6. After the adsorption step, the reactor was maintained at 45 °C for 20 to 28 min to desorb weakly adsorbed C_3H_6. Subsequently, the samples were heated to 450 °C at the rate of 10 °C/min. The desorbed gas products were continuously measured by a mass spectrometer (Pfeiffer, Prisma) to account for the release of the remaining trapped C_3H_6.

An example of the breakthrough curves for C_3H_6 adsorption and desorption on beta-zeolite is depicted in Figure 2. In this case, the sorbent sample consisted of 0.1 g Ag-beta-zeolite and 0.3 g quartz powder. Quartz powder was added to dilute the sample and to minimize the temperature change due to adsorption exotherms. The resulting breakthrough profiles indicate that effectively 100% of the C_3H_6 was adsorbed during the 3 min step input. After 30 min, the temperature was increased at 10 °C/min. Significant desorption of C_3H_6 began at 250 °C and peaked at about 350 °C. Interestingly, this desorption temperature range for C_3H_6 would appear to be matched well with the expected activity of a downstream TWC, since TWCs are typically highly active above 250 °C.

Figure 3 illustrates an example of the combined adsorption and desorption of C_3H_6 in a mixture of sorbent materials such as might be used in a multifunctional adsorber device. In this case, the sorbent sample consisted of 0.1 g of Ag-ZSM-5, 0.1 g of Ag-beta-zeolite, and 0.1 g of Fe–Mn–Zr transition metal oxides diluted with 0.3 g of quartz powder. The feed gas also consisted of a more complex mixture of simulated exhaust species, including 320 ppm NO, 2000 ppm CO, 2000 ppm C_3H_6, 4% CO_2, 2% H_2O, 2% O_2 with a balance of argon. The C_3H_6 adsorption and desorption by Ag-beta-zeolite was still effective, although the initial breakthrough during the capture phase appears to be slightly increased. Under the mixed-gas conditions, C_3H_6 desorption still began at 250 °C and peaked at 350 °C (see Figure 3).

Adsorption model

Relatively simple kinetic models of adsorption and desorption have been demonstrated to be widely useful for modeling industrial sorption processes.[22] For simulating a passive automotive adsorber device, we used one-dimensional transient differential mass and energy balances. We also utilized a transient energy balance along the same lines as the lean NO_x trap model published previously[23] to account for variations in the gas temperature. Details of the energy balance are available in Appendix 2. In the present model, the heats of adsorption and desorption are not accounted for in the energy balance since they are relatively small compared with the sensible exhaust heat, but they can easily be added.

For the present model, we assumed that the rate-limiting steps are first order with respect to gas concentrations and adsorption site coverage. We further assume that there are two distinct reversible adsorption steps involving each adsorbing species A of interest and a competing adsorption process for H_2O according to

$$A + S_A \leftrightarrow A - S_A \quad (1)$$

$$H_2O + S_A \leftrightarrow H_2O - S_A \quad (2)$$

Net adsorption and desorption rates for the above processes are then determined as

$$R_{A-S_A} = k_{A-S_A,f} C_A (1 - \theta_{A-S_A} - \theta_{H_2O-S_A}) \psi_A - k_{A-S_A,b} \theta_{A-S_A} \psi_A \quad (3)$$

$$R_{H_2O-S_A} = k_{H_2O-S_A,f} C_{H_2O}(1 - \theta_{A-S_A} - \theta_{H_2O-S_A})\psi_A - k_{H_2O-S_A,b}\theta_{H_2O-S_A}\psi_A \quad (4)$$

where C_A is the gas-phase concentration of the adsorbing species, C_{H_2O} is the gas-phase concentration of water, and θ_{A-S_A} and $\theta_{H_2O-S_A}$ are the fractional coverages of the adsorbing species and water respectively on the available sorbent sites. The parameter ψ_A is the total adsorbent storage capacity per unit catalyst volume, which was already known from our HC experiments. We assume that the forward (adsorbing) rate constants $k_{A-S_A,f}$ and $k_{H_2O-S_A,f}$ and backward (desorbing) rate constants $k_{A-S_A,b}$ and $k_{H_2O-S_A,b}$ have Arrhenius relationships with temperature (i.e. $k = k_0\, e^{-E_A/RT}$, where k_0 is the pre-exponential factor and E_A is the activation energy).

At this stage, we do not attempt to account for any mass transfer effects (associated with the rate constants transport of species between the bulk gas and sorbent surface or within the sorbent itself), although these can be readily added in the future if they are found to be important. The above assumptions based on adsorption and desorption kinetics alone are similar to those proposed by other researchers.[24–26] In general, we expect that water competition with the key adsorbing species is likely to be important since the water affinity of many typical sorbents is high and the water concentrations in the engine exhaust are typically not less than 8 mol %.

As an initial guess, we assume that the activation energies for both forward adsorption steps are effectively zero, which is consistent with some other studies.[24,25] With this assumption, it is still necessary to specify the pre-exponential factors for both the adsorption steps and to specify the pre-exponential factors and activation energies for both the desorption steps in order to simulate the adsorption dynamics. Using the experimental measurements for HC adsorption described above, we estimated the rate parameter values summarized in Table 1. While these kinetic parameter values give good agreement with our measurements as illustrated in Figure 3, they should still be considered preliminary since they are based on a rather limited number of experimental data. In particular, it is likely that utilization of the coverage-dependent activation energies will be useful, as it has been for modeling ammonia adsorption in selective catalytic NO_x reduction.[27]

Only a very limited number of data are available in the literature for estimating the kinetics of NO_x adsorption by transition metal oxides, and we were unable to obtain confirmed experimental measurements of these materials for this study. Instead, we decided to investigate the sensitivity of NO_x trapping (focusing on just NO for now) to the assumed sorbent properties using the general model described earlier. We accomplished this by defining three different combinations of pre-exponential factors and activation energies associated with NO desorption (Table 2) to obtain some sense of how these parameters affect the trapping performance predicted by the model. As illustrated in Figure 4, our choice of these parameters causes the predicted NO breakthrough profiles to exhibit three distinct shapes. When there is competition with H_2O (kinetic sets I and III in Table 2), the breakthrough profiles exhibit bimodal shapes that reflect peaks in the NO release rate at two different temperatures. When the coverage-dependent activation energy for NO release is not included (kinetic sets II and III), the

Table 1. Kinetic parameters used for simulating passive HC adsorption.

Rate constant (unit)	Pre-exponential factor (mol/m^3 s)	Activation energy (J/mol)
$k_{C_3H_6-S_{HC},f}$	0.94	0
$k_{C_3H_6-S_{HC},b}$	1.002×10^9	135.37×10^3
$k_{H_2O-S_{HC},f}$	1.256×10^{-3}	0
$k_{H_2O-S_{HC},b}$	1.0×10^{11}	82.5×10^3

Table 2. Kinetic parameters employed for simulating passive NO adsorption.

Rate constant (unit)		Pre-exponential factor (mol/m^3 s)	Activation energy (J/mol)
Kinetic set I	$k_{NO-S_{NO_x},f}$	1.19	0
	$k_{NO-S_{NO_x},b}$	6.5×10^3	69.81×10^3 [1 − 0.18 ($\theta_{NO-S_{NO_x}}$ + $\theta_{H_2O-S_{NO_x}}$)]
	$k_{H_2O-S_{NO_x},f}$	13.95×10^{-3}	0
	$k_{H_2O-S_{NO_x},b}$	1.0×10^{11}	139.62×10^3
Kinetic set II	$k_{NO-S_{NO_x},f}$	1.19	0
	$k_{NO-S_{NO_x},b}$	6.5×10^3	69.81×10^3
	$k_{H_2O-S_{NO_x},f}$	0	0
	$k_{H_2O-S_{NO_x},b}$	0	0
Kinetic set III	$k_{NO-S_{NO_x},f}$	1.19	0
	$k_{NO-S_{NO_x},b}$	6.5×10^3	69.81×10^3
	$k_{H_2O-S_{NO_x},f}$	13.95×10^{-3}	0
	$k_{H_2O-S_{NO_x},b}$	1.0×10^{11}	139.62×10^3

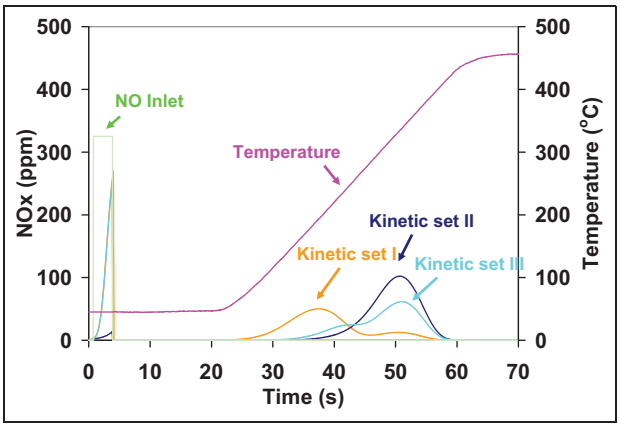

Figure 4. Simulated NO_x breakthrough curves for the fixed-bed sorber with three different sets of assumed kinetic parameters.
NO_x: nitrogen oxides.

dominant part of NO release is shifted to a higher temperature, reflecting the fact that NO becomes more strongly bound. Removing the competitive adsorption of water (i.e. kinetic set II) also tends to increase the temperature at which NO is released as well as increasing the effective NO storage capacity.

Vehicle simulations with passive adsorption after-treatment

After characterizing the breakthrough behavior of our HC and NO sorbent models, we simulated the expected emissions performance of both an HEV and a PHEV equipped with passive sorbers and operating under hybrid drive cycle conditions. We made the simulations using the PSAT with specified vehicle configurations based on the 2004 Toyota Prius drivetrain. The 1450 kg HEV configuration included a 1.5 l gasoline engine and a 1.3 kW h battery. For the HEV simulations, we assumed a charge-sustaining management strategy to eliminate off-board charging of the battery. As reported elsewhere, the baseline simulation of this HEV over a Urban Dynamometer Driving Schedule (UDDS) cycle (initiated with a cold start at 20 °C) gives excellent agreement between the predicted and experimentally measured fuel economies (30.33 km/l and 30.30 km/l respectively).[21]

For our PHEV simulations, we increased the battery capacity to 5.0 kW h and used a modified charge depletion control strategy.[21] The charge depletion mode allows the PHEV to use primarily the electrical energy until a power threshold is exceeded, which minimizes engine operation and fuel consumption. Since the PHEV battery is larger, the mass of the vehicle was increased to 1542 kg based on suggested literature values.[21] A baseline comparison of the fuel economy of this simulated PHEV (62.9 km/l) also compares well with experimental measurements (63.1 km/l), as reported elsewhere.[28] As might be expected, the PHEV operates mostly in the electric mode for the entire cycle because the battery provides all the needed power except during occasional heavy-load conditions. Consequently there are multiple periods where engine shutdown leads to exhaust temperatures below 200 °C, as reflected in the engine-out temperature and speed traces in Figure 5.

In all our simulations, we assumed that both the HEV and the PHEV were equipped with a two-stage 2.2 l (total) three-way catalytic converter. For simulations with passive adsorption, we assumed that a 0.67 l adsorber device was installed midway between the 1.1 l TWC stages, as illustrated in Figure 6. The simulated adsorber device was also assumed to have the properties of a wash-coated cordierite monolith with a cell density of 400 cells/in^2 and a void fraction of 0.7. Based on the literature values, the storage capacities of HC and NO sorbents were assumed to be 1.5 mmol/g for C_3H_6[29] and 0.80 mmol/g for NO[15] under dry

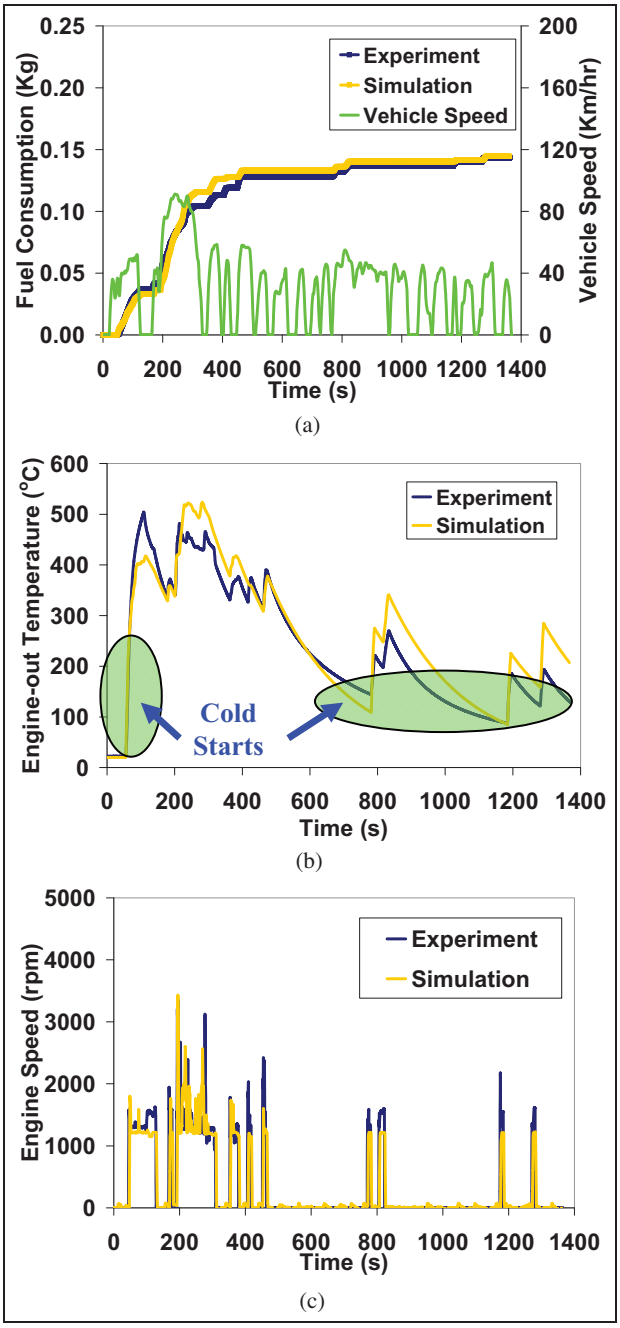

Figure 5. Comparison of the predicted and experimental fuel consumptions, engine exhaust temperatures, and engine speeds for the simulated Toyota Prius PHEV operating over a UDDS cycle (beginning with a cold start at 20 °C).

conditions. This is consistent with ψ_{HC} and ψ_{NO_x} values of 180 mol/m^3 and 60 mol/m^3 respectively. The TWC model used in this study was the same as the model that we published previously.[21]

Figure 7 and Table 3 summarize the predicted impact of a PHEV HC trap with the experimental sorbent characteristics (for C_3H_6) described earlier. The presence of the trap reduces cumulative tailpipe HC emissions by 68% from 0.052 g/km to 0.016 g/km. This difference is due largely to the adsorber's trapping of the engine-out

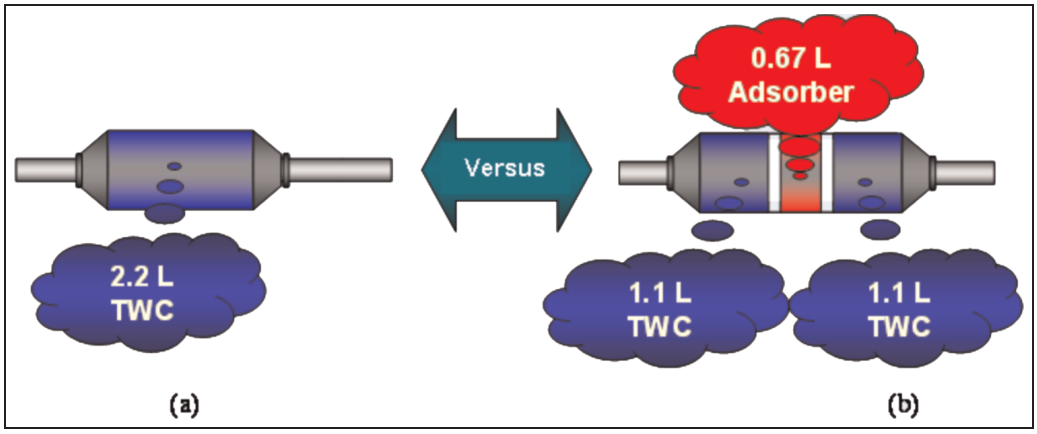

Figure 6. Conceptual schematic diagram of the two simulated configurations for the after-treatment system (with and without the adsorber).
TWC: three-way catalyst.

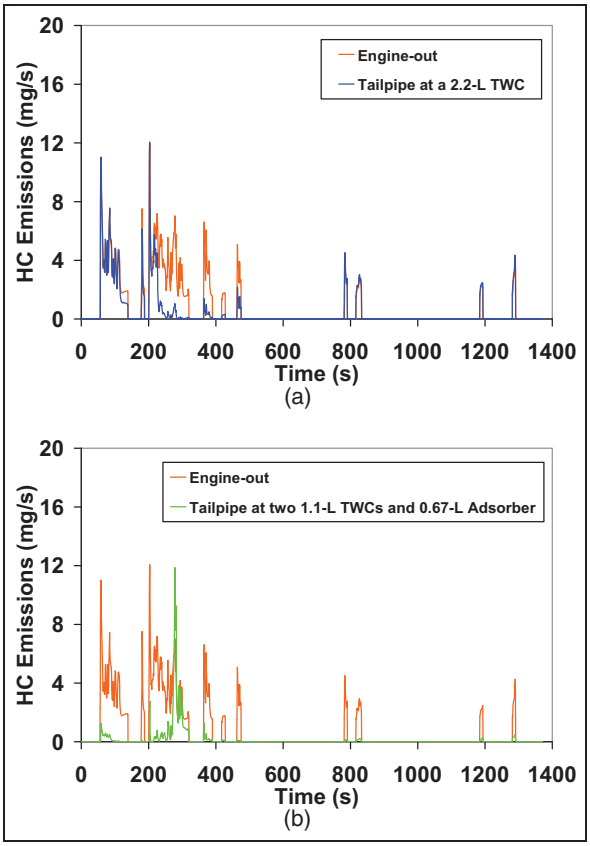

Figure 7. Simulated PHEV HC emissions with and without a passive adsorber operating over a UDDS cycle starting at 20 °C.
HC: hydrocarbon; TWC: three-way catalyst.

HC emissions during the first 200 s of the drive cycle. Moreover, after the first 600 s, there are also multiple engine restarts in which the adsorber is also effective. These effects are revealed in a different way in Figure 8, where the stored HC levels are depicted at different locations within the trap. Interestingly, at 250 s the adsorber-equipped PHEV briefly has a high HC slip at the tailpipe (Figure 7(b)). This is due to a very rapid HC desorption as the adsorber temperature increases to more than 350 °C (Figure 9).

The HEV simulations with the passive HC adsorber reveal some interesting differences from the PHEV simulations. As illustrated in Figure 10 and Table 3, the tailpipe emissions of HCs are still substantially reduced (0.033 g/km compared with 0.059 g/km without the adsorber), but the percentage emission reduction achieved by using the adsorber is less than for the PHEV (44%). One factor behind this difference appears to be the occurrences of an even larger HC desorption spike at 200 s (see Figure 10(b)). This spike is driven by a dramatic temperature increase from 150 °C to 600 °C, which does not happen for the PHEV (Figure 11).

As explained above, for our simulations of NO trapping in the HEV and the PHEV, we focused on revealing the impact of changes in the key sorbent parameters. Figures 12 and 13 compare the resulting engine-out, untrapped tailpipe, and trapped tailpipe NO emissions profiles, and Table 4 summarizes the cumulative NO_x emissions. The results show that the NO tailpipe emissions can potentially be reduced by 28–48% for the HEV and by 26–32% for the PHEV,

Table 3. Summary of the simulated cumulative HC emissions from the HEV and the PHEV.

Vehicle	Engine-out HC (g/km)	Tailpipe HC (g/km) with 2.2 l TWC	Tailpipe HC (g/km) with TWCs and adsorber
PHEV	0.089	0.052	0.016
HEV	0.231	0.059	0.033

HC: hydrocarbon; TWC: three-way catalyst; PHEV: plug-in hybrid electric vehicle; HEV: hybrid electric vehicle.

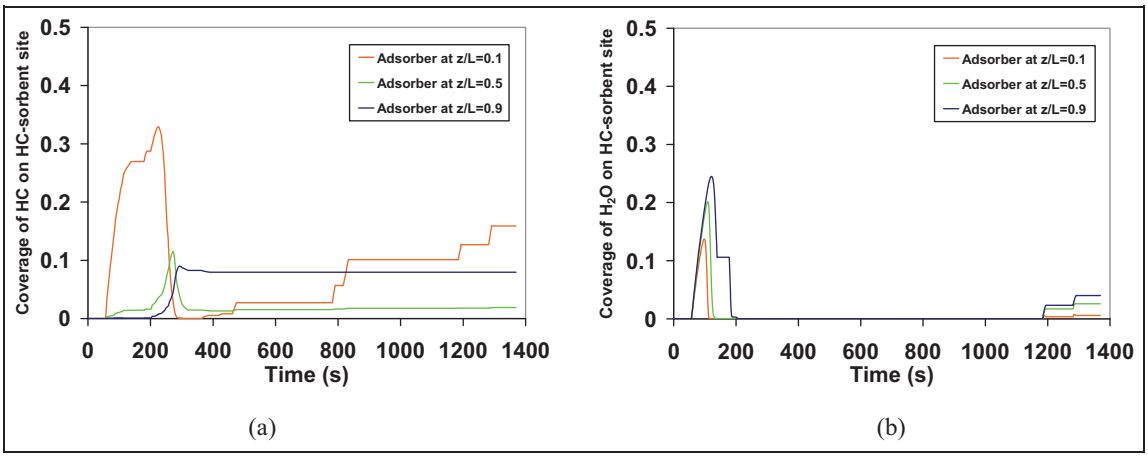

Figure 8. Transient coverage of HC and H_2O on the HC sorbent sites during the PHEV simulation.
HC: hydrocarbon.

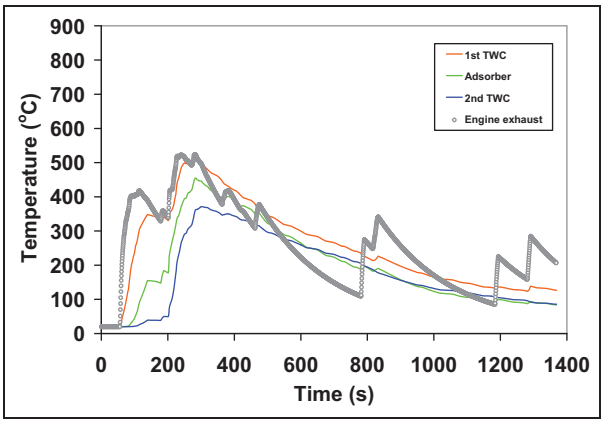

Figure 9. Simulated temperatures of the PHEV engine-out exhaust, the TWC, and the passive adsorber during the UDDS cycle.
TWC: three-way catalyst.

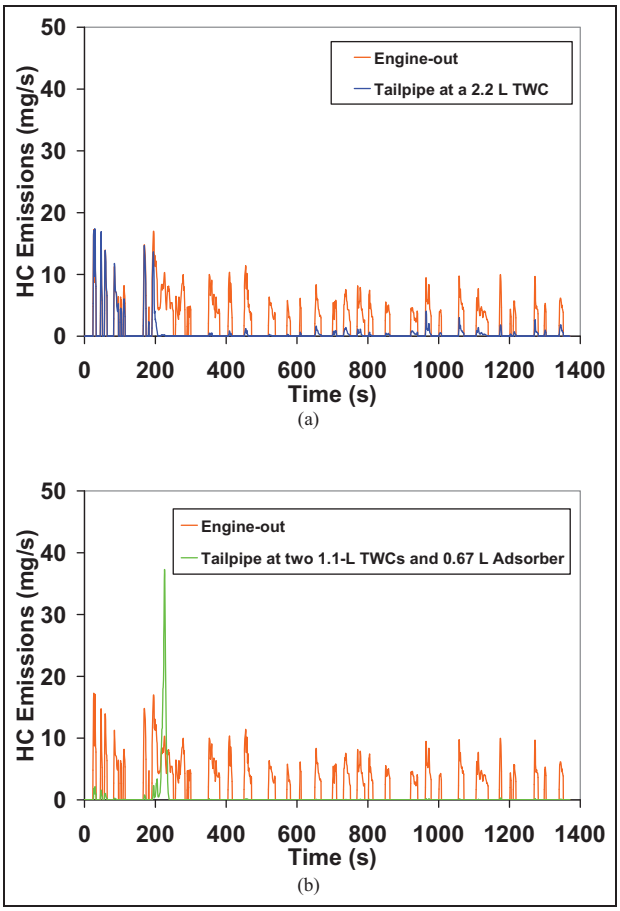

Figure 10. Simulated HEV HC emissions with and without an HC adsorber over a UDDS cycle starting at 20 °C.
HC: hydrocarbon; TWC: three-way catalyst.

for the range of assumed kinetic parameters. Also, the PHEV tailpipe emissions appear to be suppressed more effectively than those from the HEV.

The responses to the NO parameter changes also illustrate how the surface coverage effects and competitive water adsorption modify the effective NO trapping performance. In Figures 12 and 13 and Table 4 we observe that the overall NO trapping performance in both vehicles improves progressively as we advance among kinetic parameter sets I, II, and III. Kinetic parameter set II (no surface coverage term and no water competitive adsorption) achieves the best performance of the three different case studies, and kinetic parameter set III (no surface coverage term and inclusion of water competitive adsorption) also gives a better overall performance than does kinetic parameter set I. Thus it appears that the delayed NO release profiles illustrated in Figure 4 results in better TWC performance during the cold-start process. This result appears to imply that coverage-dependent adsorption of NO is likely to have a negative effect on the trapping performance, and competitive water adsorption can notably degrade the NO adsorption and TWC performance. However, the NO trapping could still be possibly beneficial if it is appropriately matched to the NO kinetic parameters.

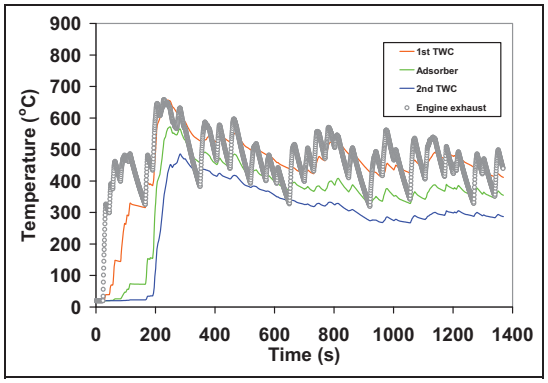

Figure 11. Simulated temperatures of HEV engine-out exhaust, TWC, and adsorber over a UDDS cycle starting at 20 °C.
TWC: three-way catalyst.

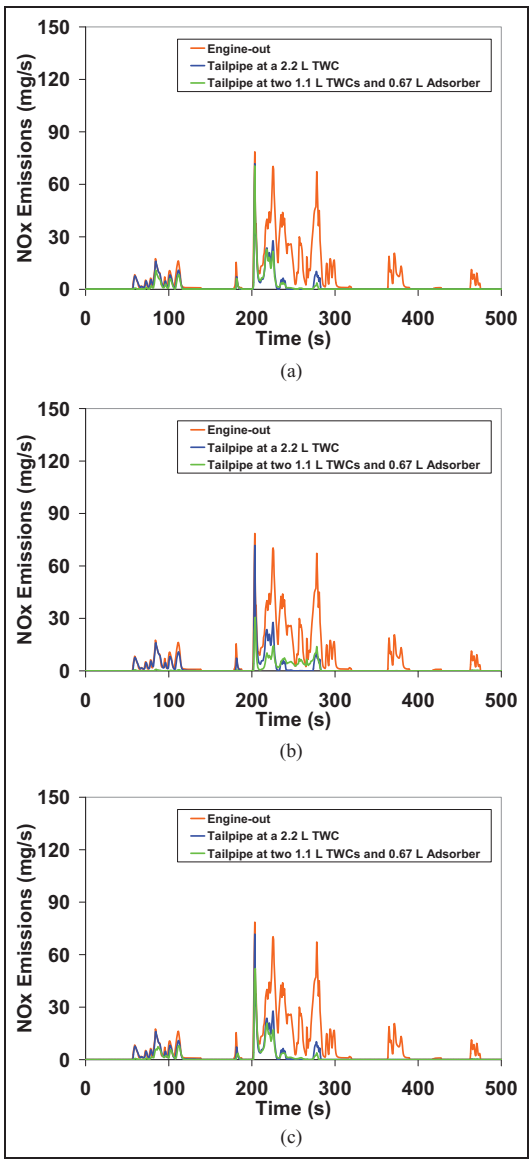

Figure 12. Transient engine-out, untrapped tailpipe, and trapped tailpipe NO emissions profiles for the PHEV simulation with the sensitive sorbent parameters: (a) kinetic set I; (b) kinetic set II; (c) kinetic set III.
NO_x: nitrogen oxides; TWC: three-way catalyst.

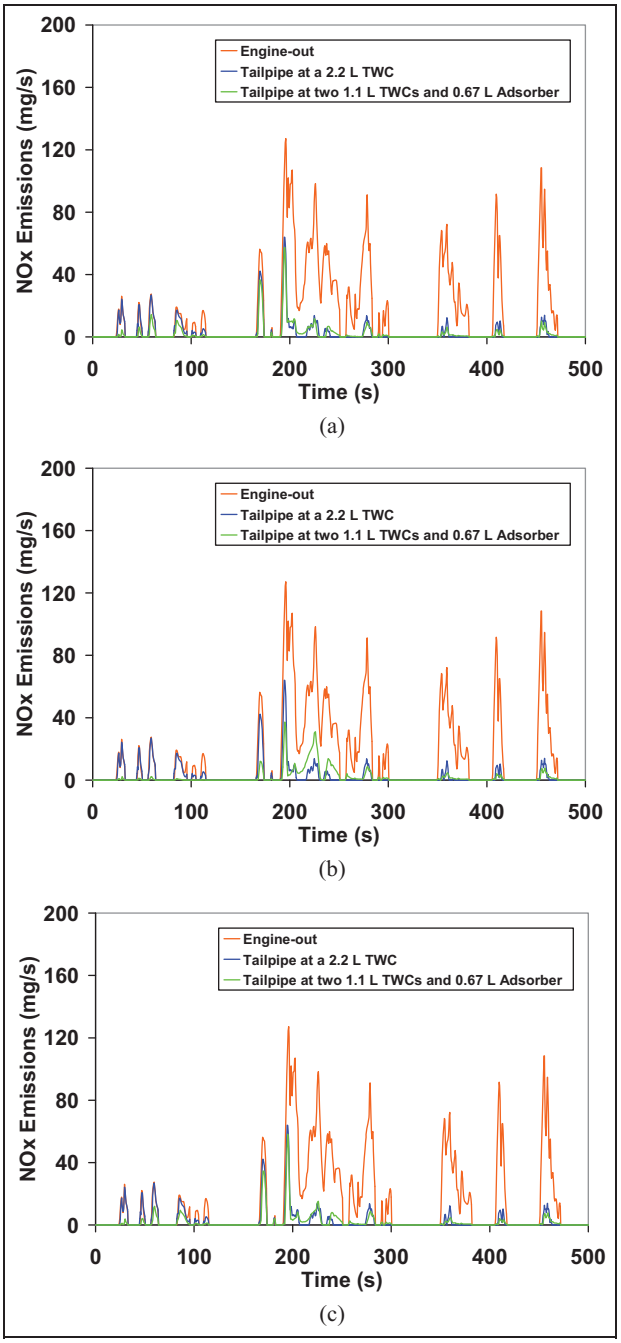

Figure 13. Transient engine-out, untrapped tailpipe, and trapped tailpipe NO emissions profiles for the HEV simulation with the sensitive sorbent parameters: (a) kinetic set I; (b) kinetic set II; (c) kinetic set III.
NO_x: nitrogen oxides; TWC: three-way catalyst.

To understand better the impact of the sorbent capacity, we also simulated PHEV and HEV cases with significantly higher capacity factors (ψ_{HC} increased from 180 mol/m^3 to 270 mol/m^3 and ψ_{NO_x} increased from 60 mol/m^3 to 120 mol/m^3). For these cases the HC and NO kinetic parameters were set at the values summarized in Table 1 and Table 2 (kinetic set I) respectively. The cumulative tailpipe emissions are summarized in Table 5. Figure 14 show examples of the impact of NO sorbent loading on the tailpipe

Table 4. Summary of the simulated cumulative NO_x emissions from the HEV and the PHEV with different assumptions concerning the kinetic parameters.

Vehicle	Engine-out NO_x (g/km)	Tailpipe NO_x (g/km) with 2.2 l TWC	Tailpipe NO_x (g/km) with TWCs and adsorber		
			Kinetic set I	Kinetic set II	Kinetic set III
PHEV	0.266	0.077	0.056	0.040	0.052
HEV	1.101	0.116	0.086	0.079	0.082

NO_x: nitrogen oxides; TWC: three-way catalyst; PHEV: plug-in hybrid electric vehicle; HEV: hybrid electric vehicle.

Table 5. Summary of the simulated impact of the HC and NO_x trap storage capacities on the cumulative HC and NO_x emissions.

Vehicle	Tailpipe HC (g/km) with TWCs and adsorber[a]	Tailpipe HC (g/km) with TWCs and adsorber[b]	Tailpipe NO_x (g/km) with TWCs and adsorber[a]	Tailpipe NO_x (g/km) with TWCs and adsorber[b]
PHEV	0.016	0.011	0.056	0.050
HEV	0.033	0.031	0.086	0.078

HC: hydrocarbon; TWC: three-way catalyst; PHEV: plug-in hybrid electric vehicle; HEV: hybrid electric vehicle.
[a]ψ_{HC} and ψ_{NO_x} are 180 mol/m^3 and 60 mol/m^3 respectively.
[b]ψ_{HC} and ψ_{NO_x} are 270 mol/m^3 and 120 mol/m^3 respectively. Kinetic parameter set I in Table 2 is used for the NO_x simulation.

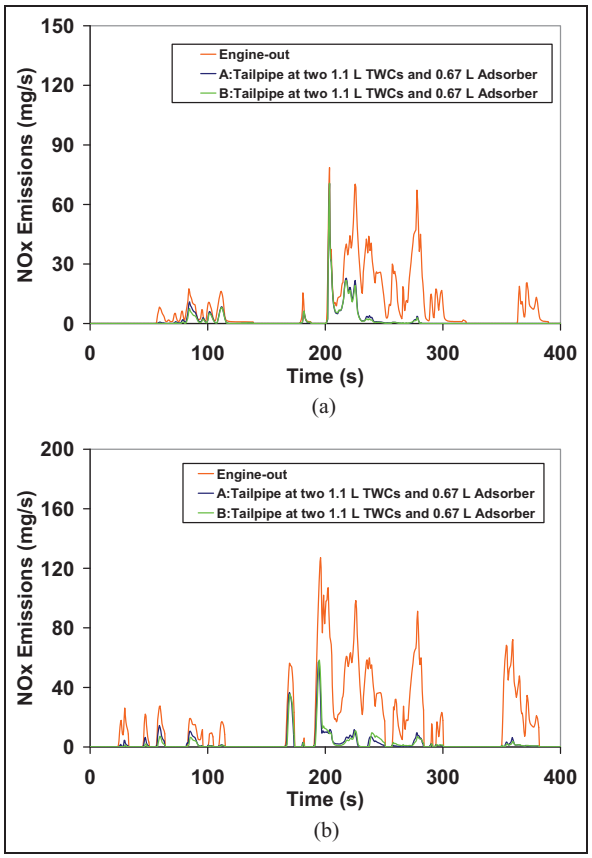

Figure 14. Impact of NO sorbent loading on (a) PHEV and (b) HEV tailpipe emissions during the first 400 s of a UDDS cycle starting at 20 °C.
NO_x: nitrogen oxides; TWC: three-way catalyst.

emissions release profiles during the first 400 s of a UDDS cycle. From these it appears that doubling the sorbent capacity is indeed beneficial, but the benefits are somewhat limited. A higher storage capacity increases the amount of emissions that can be trapped, but the storage capacity alone has little effect on the temperature at which desorption peaks. Thus it appears that the dependence of the desorption rate on the temperature (as determined by the desorption activation energy) is perhaps a more critical property.

We note finally that, in all the discussed simulations, there is no change in fuel consumption or engine operation, because the adsorber is implemented in a completely passive operating mode. The presence of the adsorber does slow the temperature response of the downstream sections of the TWC, as illustrated in Figures 9 and 11. Thus, we expect that it will be important to minimize the adsorber thermal mass to prevent adverse effects on the TWC performance.

Conclusions

Utilizing a simple adsorption and desorption model for simulating a passive HC and NO_x exhaust trapping device on an HEV and a PHEV, we observed the following.

1. Both the HC and the NO_x tailpipe emissions can potentially be reduced several fold with the appropriate combination of the sorbent properties. These improvements should be possible without suffering significant fuel penalties or requiring major changes in engine operation.
2. The relative impact of passive trapping on the emissions depends heavily on the sorbent properties, especially those which control the temperatures at which adsorbate desorption begins and reaches its peak rate.

3. The performance impact of passive adsorbers also depends heavily on the drive-cycle-dependent temperature swings. Larger benefits may be possible for PHEVs, where such swings are likely to be smaller in magnitude.
4. It appears advantageous to minimize the thermal inertia of passive trap devices in order to minimize the subsequent delay that can occur in catalyst heat-up and light-off.
5. Additional studies are needed to identify promising candidate sorbent materials and to quantify their physical properties and kinetic rate parameters. Information about potential NO sorbents appears to be especially limited.

Funding

This work was supported by the Laboratory Directed Research and Development Seed Money program (grant no. S10-055) at Oak Ridge National Laboratory and was sponsored by a contractor of the US Government under contract DE-AC05-00OR22725 with the US Department of Energy.

Acknowledgements

Forrest Jehlik and Eric Rask of Argonne National Laboratory provided helpful information regarding some of our simulation parameters for the Toyota Prius. We are also grateful to our colleagues in the Fuels, Engines, and Emissions Research Center at Oak Ridge National Laboratory who have contributed helpful suggestions and insights. The contribution of Mi-Young Kim was supported in part by an appointment to the Oak Ridge National Laboratory Postdoctoral Research Associates Program administered jointly by the Oak Ridge Institute for Science and Education and the Oak Ridge National Laboratory. We also appreciate the contribution of time and helpful comments from *Journal of Automobile Engineering* reviewers.

References

1. Yang RT. *Adsorbents: fundamental and applications*. Hoboken, NJ: John Wiley, 2003.
2. Node N, Takahashi A, Shibagaki Y and Mizuno H. In-line hydrocarbon adsorber for cold start emissions – Part II. SAE paper 980423, 1998.
3. Chan SH and Hoang DL. Heat transfer and chemical reactions in exhaust system of a cold-start engine. *Int J Heat Mass Transfer* 1999; 42(22): 4165–4183.
4. Holder R, Bollig M, Anderson DR and Hochmuth JK. A discussion on transport phenomena and three-way kinetics of monolithic converters. *Chem Engng Sci* 2006; 61(24): 8010–8027.
5. Guan B, Lin H, Zhu L and Huang Z. Selective catalytic reduction of NO_x with NH_3 over Mn, Ce substitution $Ti_{0.9}V_{0.1}O_{2-\delta}$ nanocomposites catalysts prepared by self-propagating high-temperature synthesis method. *J Phys Chem C* 2011; 115(26): 12 850–12 863.
6. Burch SD, Potter TF, Keyser MA, et al. Reducing cold-start emissions by catalytic converter thermal management. SAE paper 950409, 1995.
7. Coppage GN and Bell SR. Use of an electrically heated catalyst to reduce cold-start emissions in a bi-fuel spark ignited engine. *Trans ASME, J Eng Gas Turbines Power* 2001; 123(1): 125–131.
8. Karkanis AN, Botsaris PN and Sparis PD. Emission reduction during cold start via catalyst surface control. *Proc IMechE Part D: J Automobile Engineering* 2004; 218(11): 1333–1340.
9. Wang W, Jess RB, Hamilton LE, et al. *Method for on-board diagnosis of cold start emissions reduction control strategy*. US Patent 6871136, 2005.
10. Maier CM and Belton DN. *Control system for cold start emissions reduction in hybrid vehicles*. US Patent 0199560, 2009.
11. Lopez N, Janssens, TVW, Clausen BS, et al. On the origin of the catalytic activity of gold nanoparticles for low-temperature CO oxidation. *J Catal* 2004; 223(1): 232–235.
12. Pillai UR and Deevi S. *Gold–ceria catalyst for oxidation of carbon monoxide*. US Patent 7560410, 2009.
13. Sarshar Z, Zahedi-Niaki MH, Huang Q, et al. S. MTW zeolites for reducing cold-start emissions of automotive exhaust. *Appl Catal B – Environ* 2009; 87(1–2): 37–45.
14. Ballinger TH and Andersen PJ. *Hydrocarbon trap/catalyst for reducing cold-start emissions from internal combustion engines*. US Patent 6617276, 2003.
15. Huang HY and Yang RT. Removal of NO by reversible adsorption on Fe–Mn based transition metal oxides. *Langmuir* 2001; 17(16): 4997–5003.
16. Rabo JA, Francis JN and Angell CL. *Adsorption of carbon monoxide using silver zeolites*. US Patent 4019880, 1977.
17. Patil MD, Peng YL and Morse KE. Airless in-line adsorber system for reducing cold start HC emissions. SAE paper 980419, 1998.
18. Yamazaki H, Endo T, Ueno M and Sugaya S. Research on HC adsorption emission system. SAE paper 2004-01-1273, 2004.
19. Argonne National Laboratory, Transportation Technology R&D Center. PSAT (Powertrain System Analysis Toolkit), http://www.transportation.anl.gov/modeling_simulation/PSAT/ index.html (September 2010, accessed 8 September 2011).
20. Gao Z, Conklin JC, Daw CS, et al. A proposed methodology for estimating transient engine-out temperature and emissions from steady-state maps. *Int J Engine Res* 2010; 11(2): 137–151.
21. Gao Z, Chakravarthy VK and Daw CS. Comparisons of the simulated emissions and fuel efficiencies of diesel and gasoline hybrid electric vehicles. *Proc IMechE Part D: J Automobile Engineering* 2011; 225(7): 944–959.
22. Do DD. *Adsorption analysis: equilibria and kinetics*. Singapore: Imperial College Press, 1998.
23. Gao Z, Chakravarthy K, Daw C and Conklin J. Lean NO_x trap modeling for vehicle systems simulations. *SAE Int J Fuels Lubr 2010*; 3(1): 468–485.
24. Koltsakis GC and Stamatelos AM. Modeling of hydrocarbon trap systems. SAE paper 2000-01-0655, 2000.
25. Sampara CS, Bissett EJ and Assanis D. Hydrocarbon storage modeling for diesel oxidation catalysts. *Chem Engng Sci* 2008; 63(21): 5179–5192.

26. Kryl D, Kočí P, Kubíček M, et al. Catalytic converters for automobile diesel engines with adsorption of hydrocarbons on zeolites. *Ind Engng Chem Res* 2005; 44(25): 9524–9534.
27. Olsson L, Sjövall H and Blint RJ. A kinetic model for ammonia selective catalytic reduction over Cu-ZSM-5. *Appl Catal B: Environ* 2008; 81(3–4): 203–217.
28. Jehlik F. Methodology and analysis of determining plug-in hybrid engine thermal state and resulting efficiency. SAE paper 2009-01-1308, 2009.
29. Park J-H, Park SJ, Ahn HA, et al. Promising zeolite-type hydrocarbon trap catalyst by a knowledge-based combinatorial approach. *Microporous Mesoporous Mater* 2009; 117(1–2): 178–184.

Appendix 1

Notation

A	adsorbing species of hydrocarbons or nitric oxide
c_{pg}	specific heat of the exhaust gas (J/kg K)
c_{ps}	specific heat of the solid wall (J/kg K)
C_A	gas-phase concentration of the adsorbing species A (mol/m^3)
C_i	gas-phase concentration of species i (mol/m^3)
D_h	characteristic diameter of the adsorber channel flow (m)
E_A	activation energy (J/mol)
G_a	external heat transfer surface per volume (m^{-1})
G_m	surface area per volume of the monolith (m^{-1})
h_a	heat transfer coefficient between the ambient atmosphere and the catalyst (W/m^2 K)
h_g	laminar-flow heat transfer coefficient (W/m^2 K)
k	reaction rate constant (mol/m^3 s)
k_s	thermal conductivity of the solid wall (W/m K)
k_0	pre-exponential factor (mol/m^2 s or mol/m^3 s)
$\dot{m}_g$	exhaust-gas mass flow rate (kg/s)
Nu	Nusselt number
Pr	Prandtl number
R	universal gas constant = 8.314 J/mol K
R^k	k-step chemical reaction rate (mol/m^3 s)
Re	Reynolds number
S	frontal surface area in the converter (m^2)
Sc	Schmidt number
Sh	Sherwood number
t	time (s)
T	temperature (K)
T_a	ambient temperature (K)
T_g	exhaust-gas temperature (K)
T_s	solid-wall temperature (K)
u_g	exhaust-gas velocity (m/s)
z	moving direction of the flow (m)
α_i^k	stoichiometric coefficient of species i in the k-step chemical reaction
ΔH^k	heat generated at the k-step reaction (J/mol)
ε	void fraction of the monolith (dimensionless)
θ_{A-S_A}	coverage of A on the species A storage sites (dimensionless)
$\theta_{H_2O-S_A}$	coverage of water on the species A storage sites (dimensionless)
$\theta_{NO-S_{NO_x}}$	coverage of nitric oxide on the nitrogen oxide storage sites (dimensionless)
$\theta_{H_2O-S_{NO_x}}$	coverage of water on the nitrogen oxide storage sites (dimensionless)
ρ_g	mass density of the exhaust gas (kg/m^3)
ρ_s	density of the solid wall in the catalyst (kg/m^3)
ψ_A	storage capacity of the adsorbing species (mol/m^3)
ψ_{HC}	hydrocarbon storage capacity (mol/m^3)
ψ_{NO_x}	nitrogen oxide storage capacity (mol/m^3)

Superscripts

k	k-step chemical reaction

Subscripts

a	ambient
A	adsorbing species A
b	back
f	forward
g	exhaust gas
i	species i
s	substrate
S_A	sorbent site for species A

Appendix 2

The trap models used here were developed along the same lines as the lean NO_x trap model published previously, to account for the effect of the temperature changes on the catalyst activity and the gas species balance.[23] The gas-phase energy governing equation is defined as

$$\rho_g c_{pg} \varepsilon \left(\frac{\partial T_g}{\partial t} + u_g \frac{\partial T_g}{\partial z} \right) = h_g G_m \left(T_s - T_g \right) \tag{5}$$

where ρ_g and c_{pg} are the gas mass density and the specific heat respectively, ε is the void fraction of the monolith, G_m is the specific surface area per volume of the monolith, h_g is the heat transfer coefficient in a fully developed laminar flow, u_g is the exhaust-gas velocity expressed by $u_g = \dot{m}_g / \rho_g \varepsilon S$, where $\dot{m}_g$ is the exhaust-gas mass flow rate, ε is the void fraction of the monolith, and S is the frontal surface area in the converter.

The solid-phase energy governing equation can be described as

$$\rho_s c_{ps}(1-\varepsilon)\frac{\partial T_s}{\partial t} = k_s(1-\varepsilon)\frac{\partial^2 T_s}{\partial z^2} + h_g G_m(T_g - T_s) + h_a G_a(T_a - T_s) + \sum_{k=1}^{n} R^k \Delta H^k \tag{6}$$

where ρ_s, c_{ps}, and k_s are the density, the specific heat, and the thermal conductivity respectively of the solid wall in the catalyst, T_a is the ambient temperature, h_a is the heat transfer coefficient between the ambient temperature and the exterior surface of the catalyst, G_a is the specific external heat transfer surface per volume, R^k is the k-step chemical reaction rate, ΔH^k is the heat generated at the chemical reaction k, and L is the length of the device.

The gas-phase species governing equation is expressed as

$$\frac{\partial C_i}{\partial t} + u_g \frac{\partial C_i}{\partial z} = \frac{1}{\varepsilon}\sum_k \alpha_i^k R^k \tag{7}$$

where C_i is the mole fraction of species i in the gas phase and α_i^k is the stoichiometric coefficient of species i in the k-step chemical reaction.

The exhaust flow is considered as a fully developed laminar flow, where the heat and mass transfer coefficients in equations (5) to (7) are determined by the Nusselt number and the Sherwood number, which are given by

$$Nu = Nu_0\left(1 + 0.095\, Re\, Pr\, \frac{D_h}{z}\right)^{0.45} \tag{8}$$

$$Sh = Sh_0\left(1 + 0.095\, Re\, Sc\, \frac{D_h}{z}\right)^{0.45} \tag{9}$$

where Re is the Reynolds number, Pr is the Prandtl number, Sc is the Schmidt number, $Nu_0 = 3.657$, and $Sh_0 = 4.364$ in the above equations.